Metals and Materials International (2023) 29:369–380
https://doi.org/10.1007/s12540-022-01233-5

Characterization and Comparison of TiN Coatings Deposited on Coarse- and Nano-grained Substrates

Mahla Seifzadeh Omrani[1] · Mohsen Karimi[1] · Mansoor Bozorg[1]

Received: 11 February 2022 / Accepted: 24 April 2022 / Published online: 4 June 2022

Abstract
In this study, TiN layers were deposited on coarse- and nano-grained (CG and NG) AISI 301 stainless steel sheets using the Cathodic arc physical vapor deposition method. X-ray diffraction, Scanning electron microscopy, atomic force microscopy, Rockwell-C adhesion test, static contact angle test, electrochemical impedance spectroscopy, and polarization measurement were employed to characterize and compare the coatings on different substrates. Under the same coating conditions (current of 120 Amp, bias voltage of 100 V, pressure of 0.001 Torr, temperature range of 300–350 °C, and time of 90 min), much greater coating thickness was observed on the NG substrate. This was attributed to the epitaxial growth of the coatings on substrates and the difference in density of substrate grain-boundaries as high-energy nucleation sites for the TiN grains. Surface morphology observations showed a finer structure for the coating on the NG sample. Also, according to the results of the contact angle test the coating on the NG sample had more hydrophobicity, due to the higher density of the grain boundaries, and it confirmed the results of microscopic investigations. The coating layer exhibited an excellent adhesion quality to both substrates. The corrosion resistance was improved by grain refinement and also applying TiN coating so that coated NG sample had the best corrosion resistance.

Keywords Cathodic arc physical vapor deposition · TiN coating · Nano-grained structure · Electrochemical impedance spectroscopy

1 Introduction

Austenitic stainless steels (ASSs) are probably the most commonly used class of corrosion-resistant engineering alloys. ASSs have good corrosion resistance, mechanical properties, and dimensional stability after heat treatment [1]. Over the last years, submicron- and nano-grained ASSs sheets with significantly improved mechanical properties have been produced using heavy cold rolling and subsequent annealing [2–4]. In metastable ASSs, austenite is transformed to strain-induced martensite (SIM) by straining under the M_{d30} temperature. The progressive increase of martensite continues until a saturating strain. Extensive crushing of martensite during plastic straining increases the austenite nucleation sites in the subsequent reversion process. Therefore, noticeable grain refinement of austenite occurs after the reversion [3].

Titanium nitride (TiN), like other hard ceramics, has extensive applications as anti-corrosion and anti-wear coatings on industrial components [5, 6]. TiN-coated austenitic stainless steels (ASSs) have great potential applications in seawater corrosion resistance and medical devices due to their good corrosion resistance, excellent cryogenic properties, and good biocompatibility [7]. Various techniques i.e., physical vapor deposition (PVD, usually cathodic arc deposition or sputter deposition) and chemical vapor deposition (CVD), have been used for applying TiN coating on ASSs. Cathodic arc physical vapor deposition (CAPVD) is a method that takes advantage of achieving a strong bonding and enhanced film density [8, 9].

The effect of CAPVD process parameters on different characteristics of the TiN coating has been studied in previous researches [10–15]. Ali et al. [10] investigated the surface roughness of TiN coating as a function of substrate bias and temperature, deposition rate, nitrogen flow rate, and metal ion etching. They found that there are many factors

✉ Mohsen Karimi
m.karimi@shahroodut.ac.ir

[1] Faculty of Chemical and Materials Engineering, Shahrood University of Technology, Shahrood 3619995161, Iran

such as the condition of sample preparation, macro-droplets, compressive stress depending on coating thickness, and growth defects that affect the surface roughness of coating. In another study by Ali and et al. [11], it was demonstrated that the microstructure and mechanical properties of TiN have been influenced by the substrate bias voltage. They found that by increasing the substrate bias from 0 to − 150 V, the thickness of the deposited coating decreased. This was attributed to the increase in the substrate temperature and resputtering of the macroparticles at higher substrate biases. Although the effect of some coating parameters has been well documented, the effect of substrate microstructure and grain size on coating characteristics has not been investigated.

In this study, the TiN coating was applied on coarse- and nano-grained 301 stainless steel substrates using the same coating process parameters. Then the coated samples were characterized and compared together. Indeed, the effect of nanostructured 301 stainless steel substrate on coating characteristics was investigated that has not been reported before. The coatings on two different substrates were compared by microscopic inspections, XRD, Rockwell-C adhesion test, static contact angle test, and electrochemical measurement.

2 Materials and Methods

2.1 Substrate Materials

Table 1 presents the chemical composition (quantometry) of the starting material used in this study. CG sample (Starting material) was annealed sheet of 10 mm in thickness. The NG material was produced by performing heavy cold rolling and subsequent annealing [16] on the CG material. A completely martensitic structure was obtained by cold rolling operation with a 90% reduction at ambient temperature. The deformed martensite in the cold-rolled sheet was reverted to NG austenite by annealing at 850 °C for 1 min.

2.2 Sample Preparation and Coating

For the coating, CG and NG samples were cut into 30 × 10 × 1 pieces. The samples were ground with sandpaper of 2500 grit, polished with 0.03 µm alumina, and then ultrasonic cleaning was done with distilled water and ethanol. The TiN coating process was performed on the samples by the CAPVD technique. For the coating operation, 120 Amp current, 100 V bias voltage, and 0.001 Torr pressure were applied for 90 min, and the temperature range was 300–350 °C.

2.3 Characterizations

2.3.1 Microscopic Observations

To reveal the microstructure of substrates, both CG and NG samples were grounded to 2000 grit finish, polished, and electro-etched in 65% nitric acid. Scanning electron microscope (Tescan FESEM MIRA3) was employed to observe the microstructures of the CG and NG samples. ImageJ program and intercept method were used to determine the average grain size.

FESEM (model VEGA//TESCAN-LMU) and EDS analysis were used to accurately determine the thickness of the nitride coating and study the distributions of chemical elements at the surface, respectively. Also, the surface morphology was characterized using FESEM. The topography and surface roughness of the coatings were characterized via atomic force microscopy (AFM, TriboScopeTM) in non-contact mode and using a 5 mgr force. Electron backscatter diffraction analysis (EBSD) analysis was carried out by a Carl Zeiss Ultra Plus SEM equipped with a field emission gun. The working distance and operating voltage were ~ 15 mm and 20 kV and, respectively.

2.3.2 X-ray Diffraction Analysis (XRD)

XRD analysis was performed to know the presence of different phases in the coating. XRD analysis was carried out using an Asenware. AW-XDM 300 diffractometer with Cu Kα anode and 2θ measurement range of 20–80° at 0.05° step size.

2.3.3 Electrochemical Measurement

All electrochemical measurements were conducted using the biologic VSP-300 potentiostat after 30 min immersion in 3.5% NaCl solution at ambient temperature. A three-electrode cell was applied with a platinum sheet counter electrode, a saturated calomel electrode (SCE) as the reference electrode, and a 301 steel sheet as the working electrode. It should be noted that all the reported potentials in this text refer to SCE. The electrochemical impedance spectroscopy measurements (EIS) were carried out at open circuit potential over a frequency range of 100–10 mHz. The sinusoidal potential perturbation was 10 mV in amplitude. Polarization

Table 1 Chemical composition of 301 stainless steel (wt%)

C	Mn	Ni	Cr	Mo	Si	Cu	Al	Co	P	S	Nb	N
0.11	0.66	6.91	16.2	0.27	0.67	0.53	0.06	0.1	0.03	0.03 >	0.03	0.0005

curves were obtained by changing the electrode potential automatically from − 250 mV versus open circuit potential until breakdown potential with a scan rate of 1 mV/s.

2.3.4 Adhesion Test

The adhesion test was carried out on the coating using a hardness tester (KOOPA model UV1) equipped with a Rockwell C tip. 150 kg loads were used for the indentations and the level of indentation-induced cracking and coating delamination were observed with SEM and classified according to one of six categories of VDI 3198 (Fig. 1). A small number of cracks and delaminations guarantee strong interfacial bonds between the coating and the substrate. On the other hand, extended cracks and delamination in the vicinity of the imprint indicate poor interfacial adhesion. According to Fig. 1, the HF1 class includes only a small number of radial cracks without any coating delamination. HF2 category failure shows more radial cracks and there is still no spalling of the coating in the vicinity of the imprint. HF3 class is characterized by a few scattered delaminations along with radial cracks. For the HF4 class, the coating delaminations are larger but still unconnected. HF5 class shows delaminations connected in the circumferential direction at some areas of the imprint edge. For HF6 class delaminations occur all around the indentation imprint. According to this classification, indents classified as HF1 and HF2 with only radial cracks correspond to adequate adhesion, HF3 and HF4 classes are acceptable with radial cracks and minor coating delamination, while HF5 and HF6 categories with extended coating delamination around the edge of the indentation imprint are unacceptable adhesion [17].

2.3.5 Contact Angle Test

The static contact angle test was used to evaluate the surface hydrophobicity and energy of the uncoated and coated samples. The contact angle of the water sessile drop on the samples was measured using a Dataphysics-OCA30 equipment. Five different measurements were done and the mean values were reported as the contact angle of each sample.

3 Results and Discussion

3.1 Substrate Materials

The FESEM image of CG substrate is shown in Fig. 2a. According to this figure, CG substrate had a fully recrystallized and single-phase austenitic microstructure with an average grain size of 42 µm. FESEM micrograph in Fig. 2b shows that NG substrate also comprised equiaxed austenite grains. In this case, the average grain size was 260 nm. Indeed, a substantial grain refinement took place after applying the thermo-mechanical process. The EBSD grain and phase mapping are shown in Fig. 3. This figure indicates that after cold rolling and subsequent annealing, the microstructure did not completely consist of austenite grains. There was also some residual ά-martensite (BCC structure) and a little ε-martensite (HCP structure) in the structure.

3.2 Microscopic Observations of Coating

Figure 4 displays the SEM images from the cross-section of the coated samples: (a) CG, (b) NG. A compact, low-porosity layer of TiN coating with no significant defects such as cavities and cracks was formed on both substrates. Moreover, the SEM images from cross-sections did not evidence any defect or delamination at the substrate-coating interface, and a uniform thickness of the coating was formed on both substrates. However, the thickness of the coating layer in the two samples was very different. The coating thickness in NG and CG samples was estimated to be 1.8 and 0.257 µm, respectively. Figure 4 also shows EDS scans across the interface. The scanned elements were Ti, N, Fe, Cr, and Ni in the 0–10 keV energy

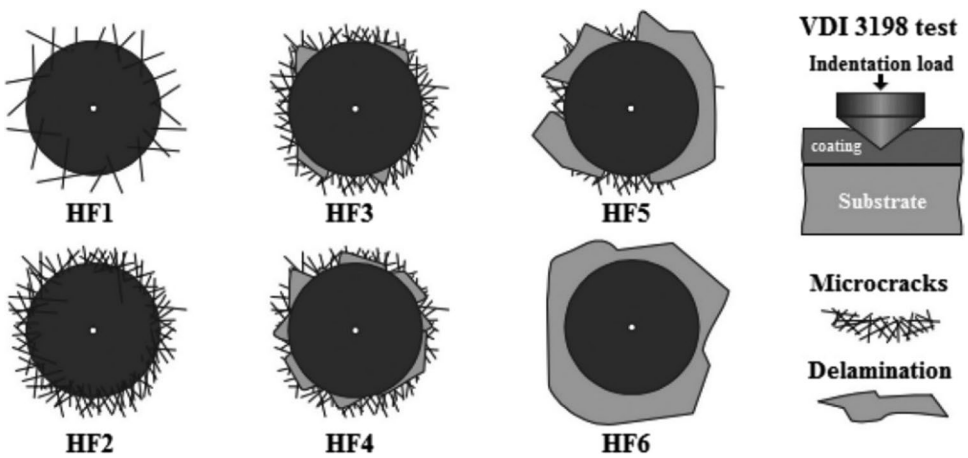

Fig. 1 Classifications of the VDI 3198 Rockwell-C adhesion test [10]

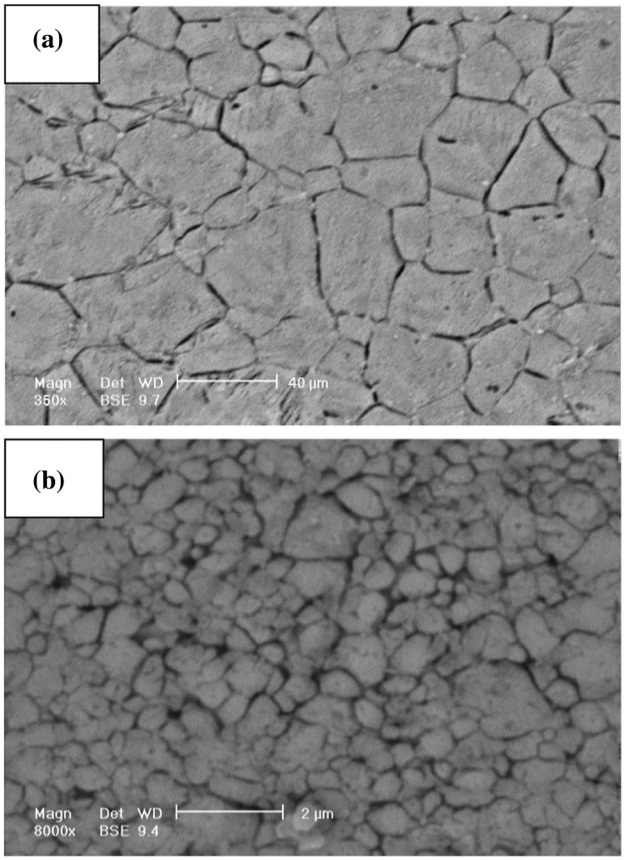

Fig. 2 FESEM micrographs of (**a**) CG and (**b**) NG substrates

range. EDS line scans were also revealing that the coating thickness for NG and CG samples was 1.8 ± 0.23 and 0.26 ± 0.05 µm, respectively. The chemical element contents of Ti and N decreased slowly at the interface, which indicated that the chemical elements had diffused from the coating to the substrate.

Changing the position of the sample within the deposition chamber can cause changes in the coating thickness. However, the position of the CG and NG samples analyzed by SEM was almost the same and such a significant difference in the coating thickness of the samples does not appear to be only due to the different positions. This significant difference can be attributed to the epitaxial growth of the coating on the substrate [18–20]. The epitaxial growth of TiN coating on the ASSs substrates has been observed in previous works. The B vector of the substrate austenite grains and large entities of small grains in TiN, called "super-grains" are identical. Therefore, TiN grows full epitaxially on the surface of the substrate [20]. Epitaxial growth can occur on both substrates with different grain sizes. Because of the smaller grain size, higher nucleation and growth rate of TiN are expected on the NG substrate. As a result, the thickness of the coating for this sample is much greater. Investigation of surface morphology (Fig. 5) also confirmed the difference between the structure of TiN films on the two substrates. According to this figure, the grain size of the coating on the NG sample was significantly smaller than that of the CG sample.

3.3 Contact Angle

The optical images of water droplet contact angle on substrates and TiN films surface are displayed in Fig. 6. A clear change in the contact angle of the droplet with the surface was observed due to the grain refinement of the substrate (Figs. 6a and b) so that the average contact angle increased from 66.7 ± 4.4 for the CG to 79.2 ± 6.1 for the NG sample. In addition, the results showed that the TiN film on the NG sample was more hydrophobic than it for the CG sample (Fig. 6c and d) so that the contact angle for the two coatings was 72.5 ± 3.6 and 94 ± 3.3, respectively. The results obtained in the contact angle test were consistent with the

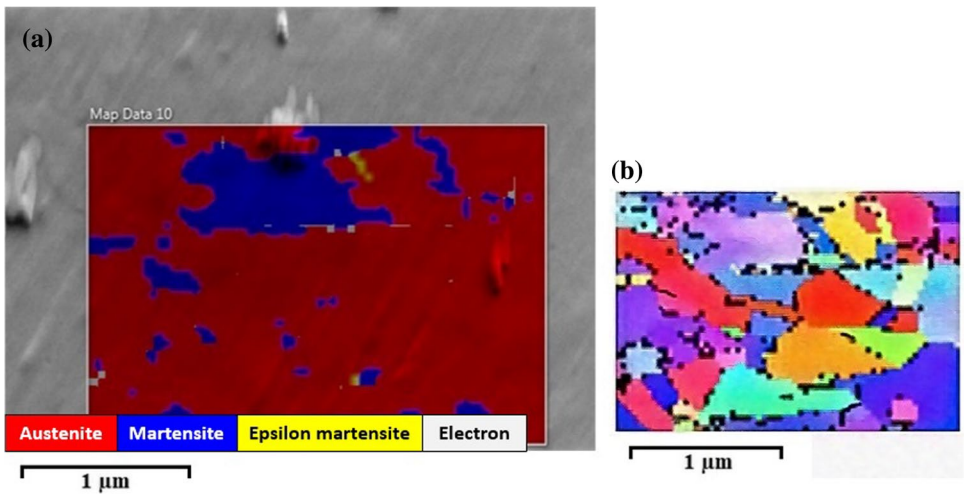

Fig. 3 The EBSD **a** phase and **b** grain maps of NG sample. The phase map shows the presence of retained ά- and ε-martensite after annealing at 850 °C for 1 min

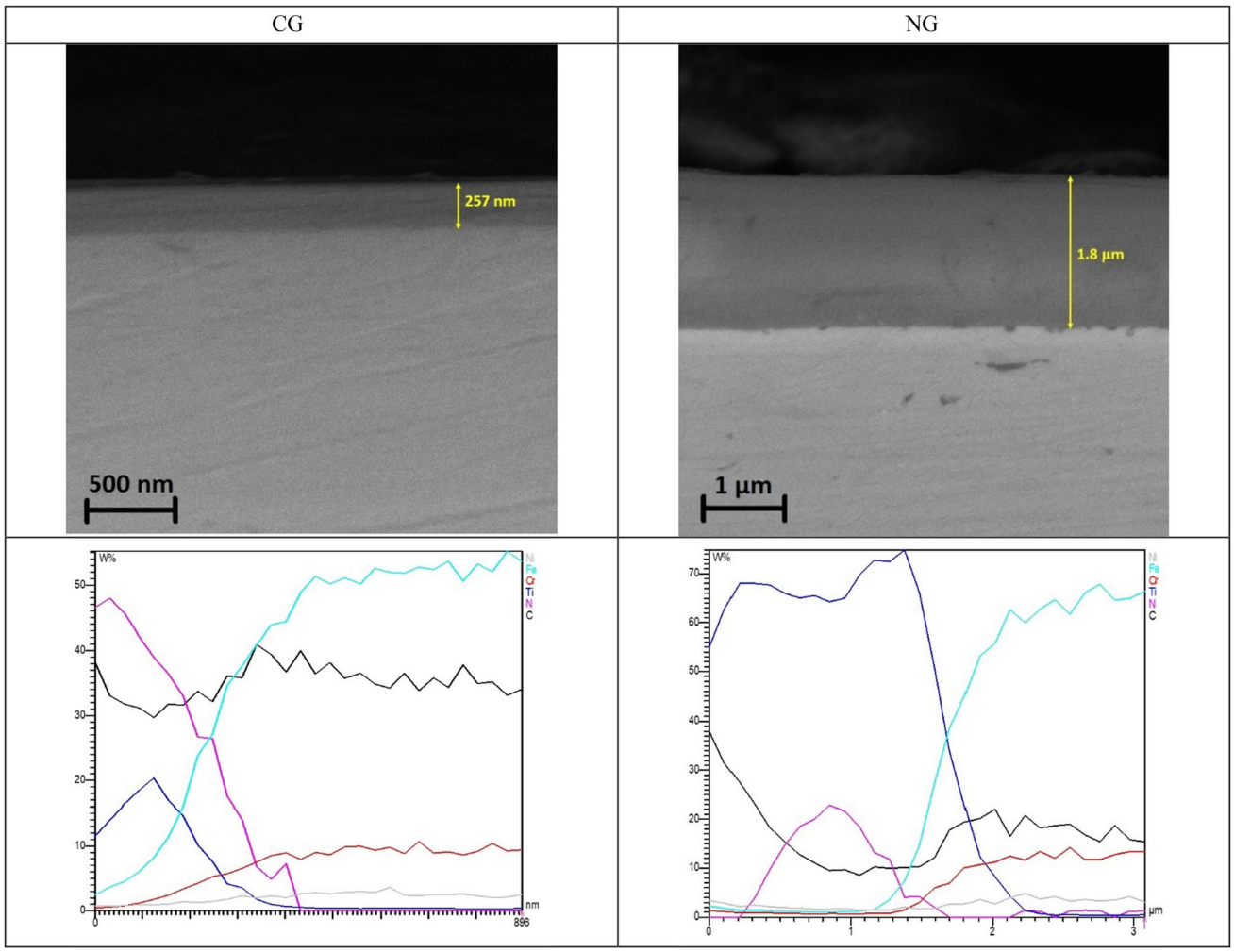

Fig. 4 SEM micrographs of the cross-section of the coated samples and EDS line-scans across the interface

results of Sect. 3–2. It can be said that when the grain size of the substrate decreased sharply, due to the huge increase in the density of the boundaries, the surface energy increased. This confirms the greater nucleation rate of TiN on the surface of the NG sample.

3.4 XRD

To confirm the presence of different phases in the samples, the XRD characterization was performed. The XRD patterns of coatings are shown in Fig. 7. The XRD pattern of the CG sample displayed (111), (200), (220), (311), and (222) reflections of TiN with a preferred orientation along the (111) plane. This was well accorded with the standard card (JCPDS card: 03-065-5759). The XRD pattern of the CG sample was also indicating the presence of an HCP Ti phase as one of the phases in the sample. This is owing to the deposition of the titanium molten droplets, which form in the cathode and move along the plasma stream to the substrate during the coating process [21]. Because of the low thickness of the coating in the CG sample, sharp reflections of the substrate austenite phase appeared in the pattern, too. In the NG sample, diffraction from (111), (200), and (222) planes of TiN again with a preferred orientation along the (111) plane was observed. In this case, the diffraction pattern also consisted of the HCP Ti and substrate austenite phase reflections. But due to the higher thickness of coating in this sample, much weaker reflections of the substrate were observed. Another noteworthy point about the XRD pattern of the NG specimen is the presence of ά-martensite reflection related to the substrate stainless steel. According to Sect. 3–1, the NG sample contained some martensite that had not reverted to austenite.

3.5 Surface Roughness and Topography of Coating

The surface roughness and topography of TiN coating were examined within the area of 5 × 5 µm. The AFM

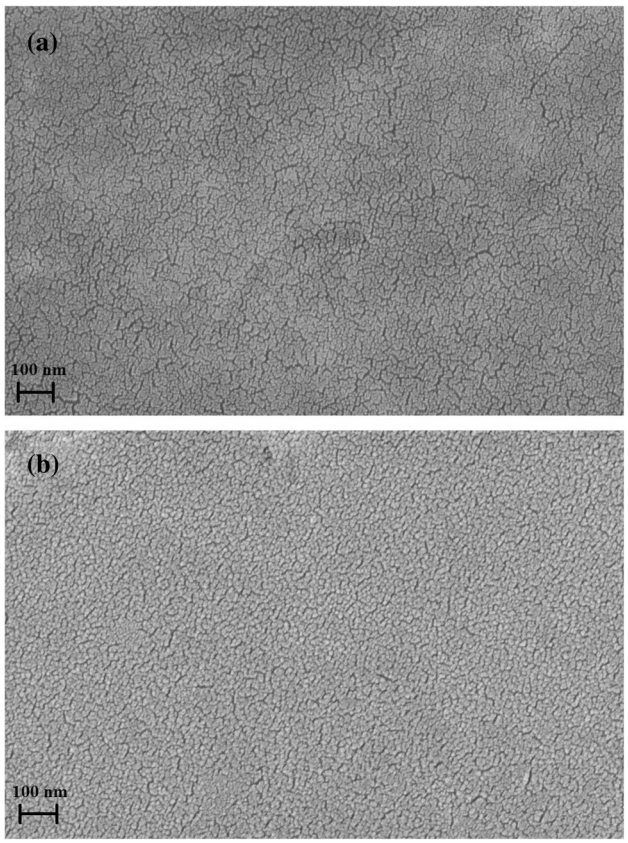

Fig. 5 SEM micrographs displaying the surface morphology of TiN coating on **a** CG and **b** NG samples

images of coatings for the CG and NG samples are shown in Fig. 8. The topography of the coating in the CG sample was smoother than that of the NG sample. The surface roughness (R_a) of the coating surface for CG and NG samples was 149 ± 11 nm and 106 ± 17 nm, respectively. The nature of the substrate and its surface [22], substrate temperature, gas pressure, coating thickness, bias voltage, and deposition time are the main parameters on which the surface roughness depends to the greatest extent [23]. Mubarak et al. [24] showed that thicker TiN coating creates more compressive stresses and therefore contributes to enhancing the surface roughness of coated metal while keeping the rest of the parameters constant. Depending on the coating parameters, previous researchers [25–28] have presented varying amounts of surface roughness (R_a parameter) in the range of ~ 50 to ~ 500 nm for TiN coating applied to austenitic stainless steels using the CAPVD method. In the present study, the substrate surface roughness, as well as the process parameters, were similar in the two samples. Although the thickness of the coating created on the NG sample was greater, it seems that the discrepancy in the surface roughness was related to the difference in the structure of the two substrates and so the difference in the structure of the coatings as described in Sect. 3–2.

3.6 Adhesion of Coating

The Rockwell-C adhesion test results are shown in Fig. 9. Two types of failures may occur in the test: (1) cohesive failure is the breaking of intermolecular bonds of the coating, and (2) adhesion failure is the separation of the coating from the substrate [29]. Indeed, Adhesive strength refers to the resistance of the coating to spalling or separating from the substrate [30]. For both tested samples, typical features were very limited radial cracks around the indent. Cohesive failure was also observed partly on the inside of the indent. Generally, good coating-substrate adhesion was observed for both samples and can be classified as HF 1.

Previous researchers have also investigated the adhesion of the TiN coating deposited on steel substrates by the PVD methods. Dalibón et al. [31] showed that the TiN coating, 1.5 µm in thickness, had excellent adhesion to a stainless steel substrate. Such that coating detachment was not observed and only some cracks could be detected around the imprint (HF1 class). In other studies, TiN coatings with less than 2 µm thickness have also shown very good adhesion (HF1–Hf2) to the steel substrates [32, 33]. At higher coating thicknesses (3.1 µm [34] and 3.8 µm [35]), relatively poorer but still acceptable adhesion (Hf2–Hf4) has been reported. However, it should be noted that other factors such as working pressure also affect the adhesion of the coating [33]. It has been demonstrated [24] that TiN coatings prepared by commercial PVD methods on steels have compressive residual stresses and with increasing the thickness, the compressive stresses also increase. Compressive stresses within the coating promote buckling and delamination of the coating and can have a detrimental effect on adhesion [36].

To evaluate the stability of the coatings, after 7 days of immersion in a 3.5% NaCl solution, Rockwell-C adhesion test was performed again on the samples. Figure 10 shows the adhesion test results after 7 immersion days. No significant changes were observed in the adhesion behavior of coating in both samples. After 7 immersion days in NaCl solution, the adhesion could also be classified as HF 1.

3.7 Electrochemical Results

Electrochemical Impedance Spectroscopy (EIS) is a suitable and powerful diagnostic method to study the electrochemical behavior and corrosion resistance of coatings. Figure 11 shows the EIS results for the NG and CG samples in coated and uncoated conditions. Nyquist plots exhibited an incomplete, large depressed semicircle of different radii, indicating an almost identical corrosion mechanism for different samples. According to previous researchers [37], a larger

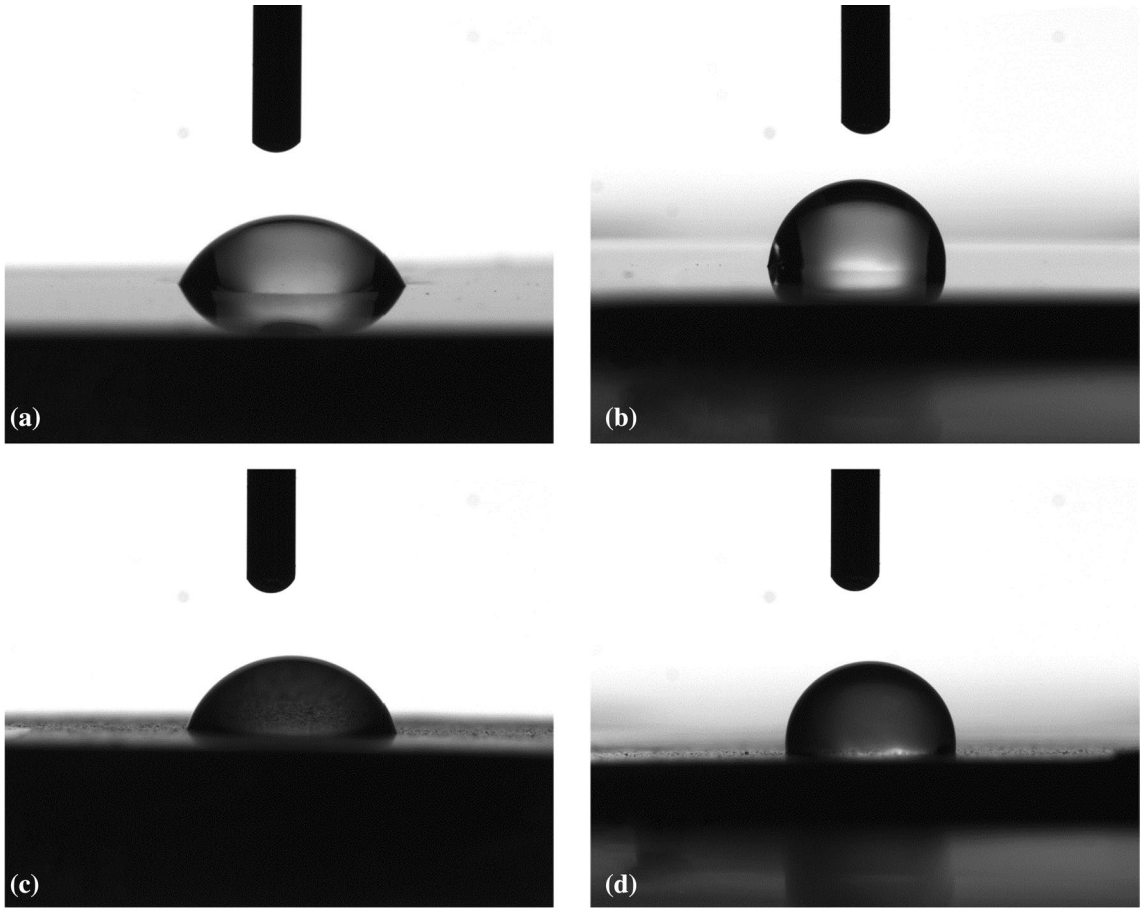

Fig. 6 Optical images of water droplets contact angle with substrates and TiN films surface; **a** uncoated CG, **b** uncoated NG, **c** coated CG, and **d** coated NG samples

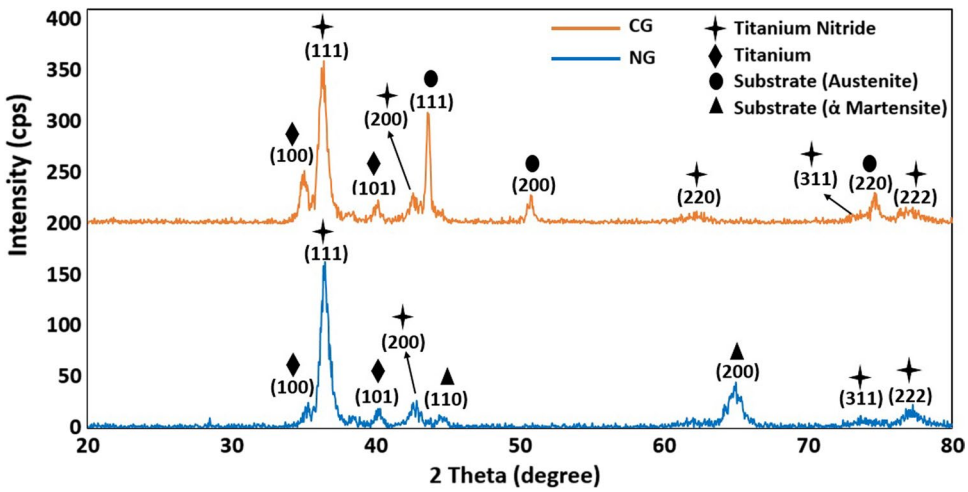

Fig. 7 Results of XRD analysis for TiN coated NG and CG samples

radius of electrochemical Nyquist plots indicates higher corrosion resistance. According to this figure, the NG sample had a slightly better corrosion resistance than the CG sample. The radius of electrochemical Nyquist plots was sharply increased by applying the TiN coating, indicating a great improvement in corrosion resistance. Also, the radius of the Nyquist plot for the coated NG sample was larger compared to the coated CG sample, which represented less penetration

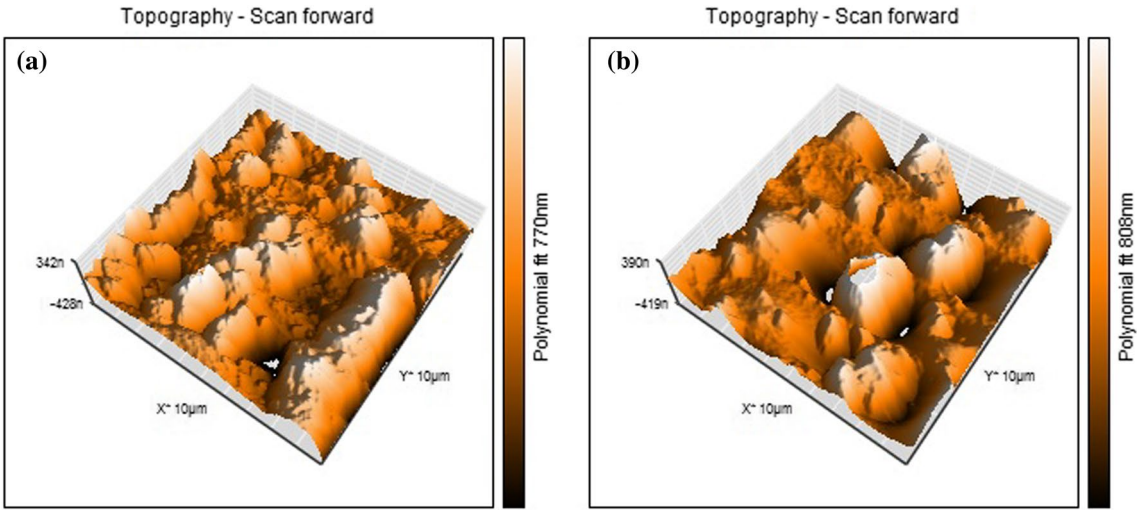

Fig. 8 Surface topography of TiN coating on **a** CG and **b** NG substrates

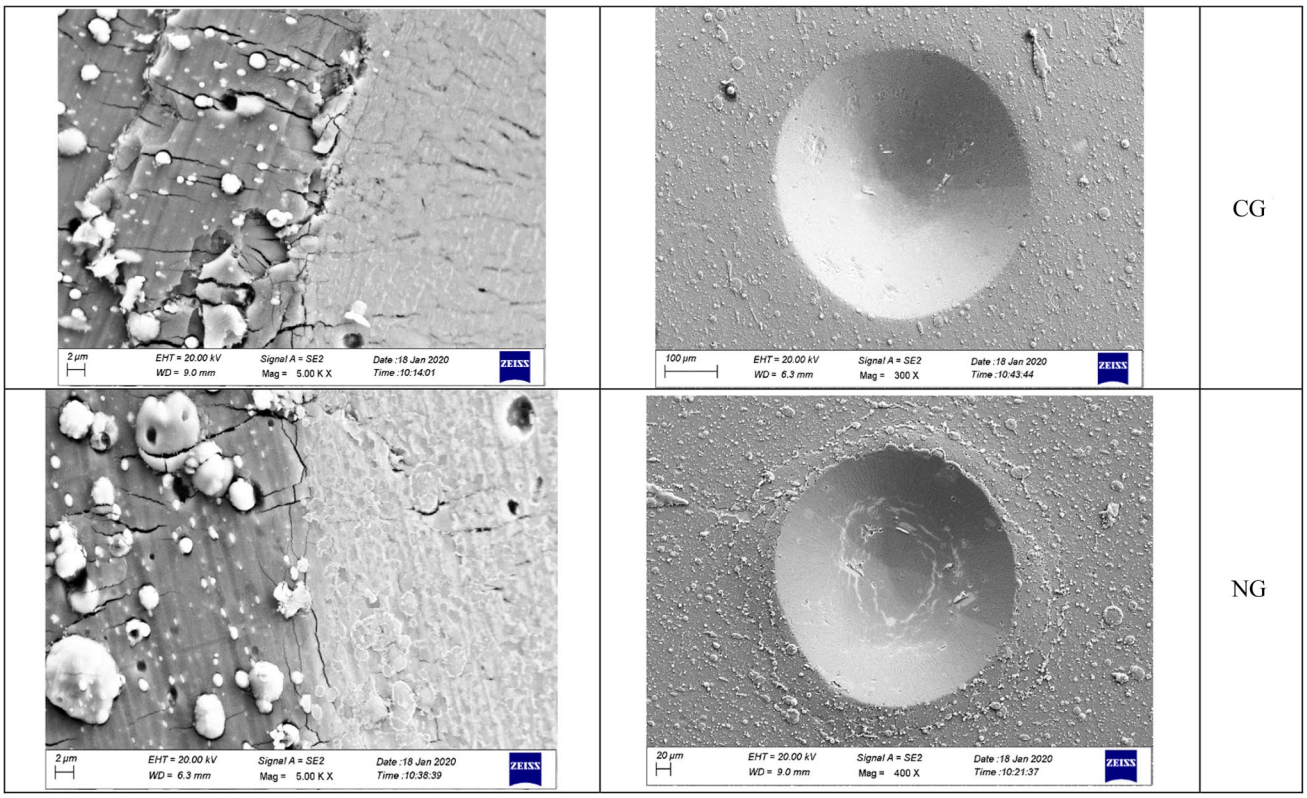

Fig. 9 SEM micrographs of the Rockwell-C indents after VDI 3198 adhesion test performed on the TiN coating

of corrosive solution in the coating and higher corrosion resistance of coated NG sample.

The equivalent circuit was used to analyze the results of the electrochemical impedance measurements (Fig. 12). In this circuit, R_s, R_f, and R_{ct} are the solution resistance, coating resistance, and charge transfer resistance, respectively. Also, CPE illustrates the constant phase element, which has replaced the ideal capacitor due to surface roughness, surface heterogeneity, etc. [38–40]. The electrochemical parameters obtained by fitting the equivalent circuit to the results of the EIS are presented in Table 2. According to this table, the values of solution resistance were almost the same for

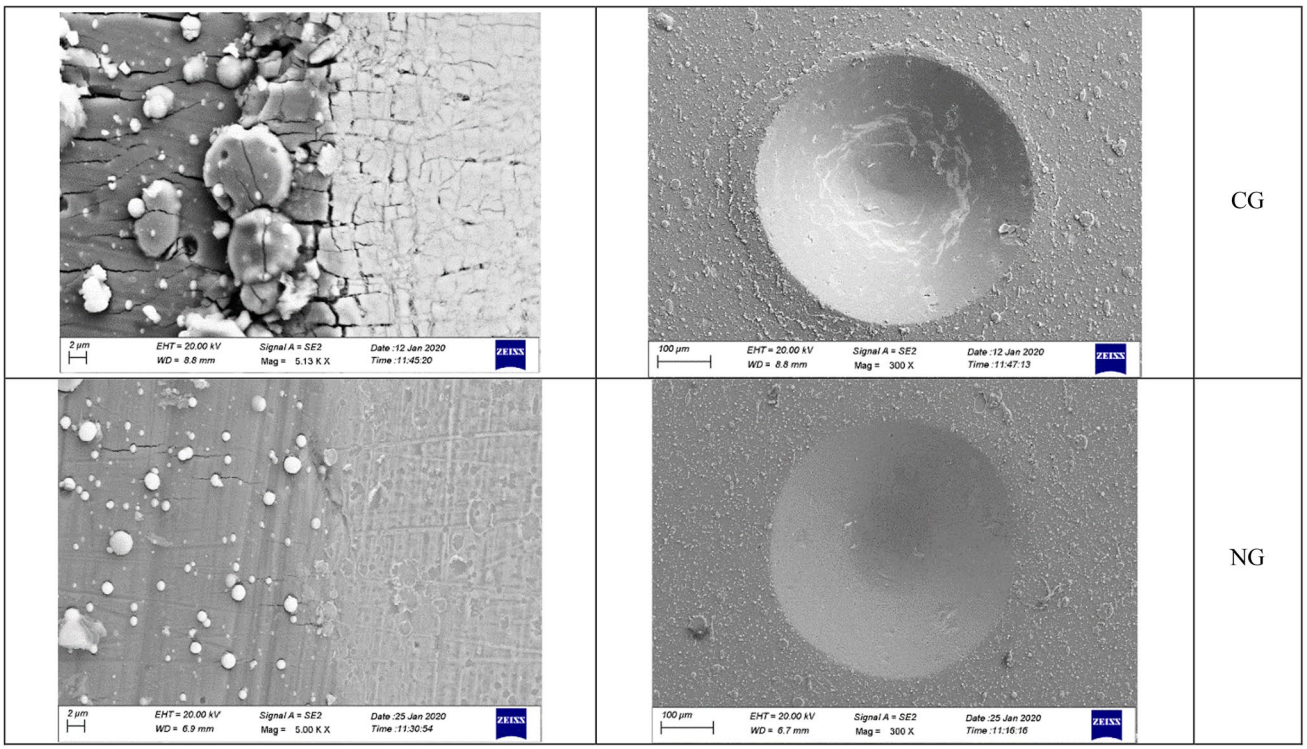

Fig. 10 SEM micrographs of the Rockwell-C indents on the TiN coating after 7 days of immersion in 3.5% NaCl

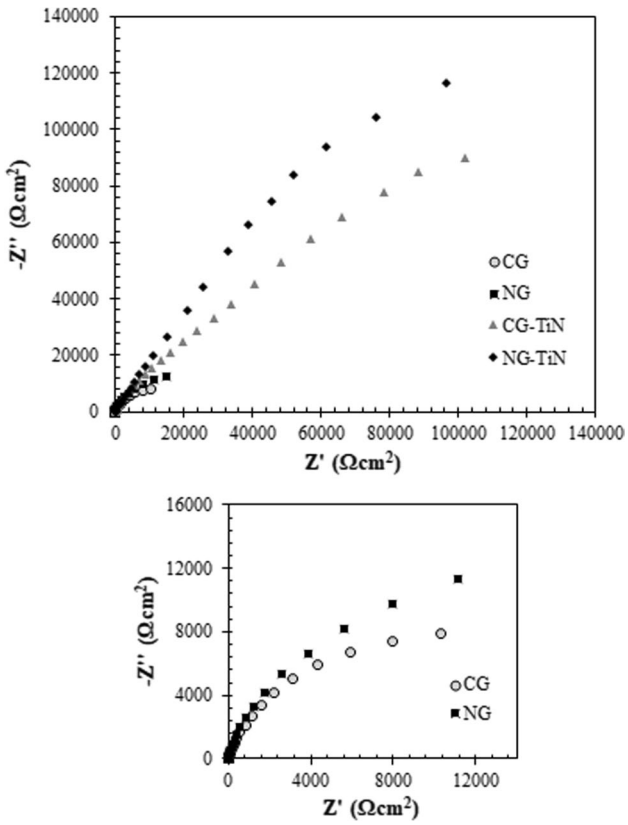

Fig. 11 Nyquist plots of CG and NG samples with and without TiN coating in 3.5% NaCl solution

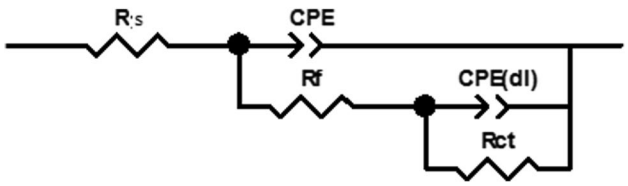

Fig. 12 Equivalent electrical circuit model used to analyse the EIS data

all samples. The charge transfer resistance increased from 18.5 to 25.4 KΩ.cm^2 owing to grain refinement from 42 to 260 nm. Ralston and Birbilis [41] in their review paper on the impact of grain size on the electrochemical behavior of different metals suggested that the effect of grain refinement on corrosion resistance is dependent on the ability of the surface to be passivated. Some researchers [42–44] believed that grain refinement provides a high density of nucleation sites for the formation of the passive film, which assists in the creation of a dense passive layer and improvement in corrosion resistance. Phadnis et al. [45] showed that the diffusion of Cr into the passive film in fine-grain samples could be increased, which resulted in a high repassivation rate. Fattah-alhosseini and Vafaeian [46] reported that the passivation behavior of AISI 430 ferritic stainless steel was enhanced by decreasing the grain size. Fu et al. [47] found that grain refining increased the corrosion resistance of pure

Table 2 Electrochemical impedance parameters for corrosion of NG and CG with and without TiN coating in 3.5% NaCl solution

Sample	R_s (Ωcm^2)	R_{ct} ($K\Omega cm^2$)	CPE_{ct} ($\mu S s^n cm^{-2}$)	n	R_f (Ωcm^2)	CPE_f ($\mu S s^n cm^{-2}$)	n
CG	6.5	18.5	602	0.88	–	–	–
NG	8.4	25.4	523	0.9	–	–	–
CG-TiN	5.3	188.9	40.4	0.85	12,040	13.7	0.83
NG-TiN	10.2	281.5	35.3	0.76	14,472	10.3	0.89

titanium. They concluded that as a result of grain refining, the corrosion resistance was enhanced which was attributed to the formation of a dense and more stable film. Other researchers illustrated that nanocrystallization induced by a surface mechanical treatment increased the corrosion resistance of AISI 409 stainless steel [48] and AISI 304 stainless steel [49]. Many studies reported that as the grains became smaller, the grain boundaries density increased, making it easier for chromium to diffuse the surface, resulting in the formation of a passive film containing chromium [50–52]. Therefore, in the NG sample, a more resistive film was formed on the surface, which prevents charge transfer reactions and increased the charge transfer resistance.

By applying the coating, the charge transfer resistance was increased significantly. The NG sample with TiN coating had the highest charge transfer resistance and thus the best corrosion resistance among the samples. Indeed, the coating acted as a barrier, and the access of corrosive ions to the substrate surface and thus the speed of anodic reaction was reduced.

The differences in the corrosion resistance of the TiN coatings could be attributed to differences in their contact angle. A correlation between wettability and anti-corrosion performance is reported [53, 54]. Teschke et al. demonstrated that the samples with more hydrophobicity are generally more corrosion resistant in aqueous environments [55]. So, according to the results of contact angle, better corrosion resistance of coated NG sample is ascribed to the more contact angle. Furthermore, as mentioned before, due to the epitaxial growth of the coating on the substrates, the coating formed on the NG sample was thicker compared with the CG sample. As the coating thickness increases, less corrosive ions penetrate and less surface area of the substrate is exposed to the corrosive solution. The lower CPE_f for the NG-TiN compared to the CG-TiN sample also confirms this.

Figure 13 shows the electrochemical polarization curves obtained in sodium chloride solution for different samples. All curves had a similar shape with a passive zone. The polarization curve for NG was slightly higher than it for the CG sample, indicating a more positive corrosion potential of the NG. With grain refinement, the electrochemical polarization curve shifted slightly to the left, and the current density decreased. Indeed, grain refinement increased the grain boundary area and as a result, the penetration of chromium

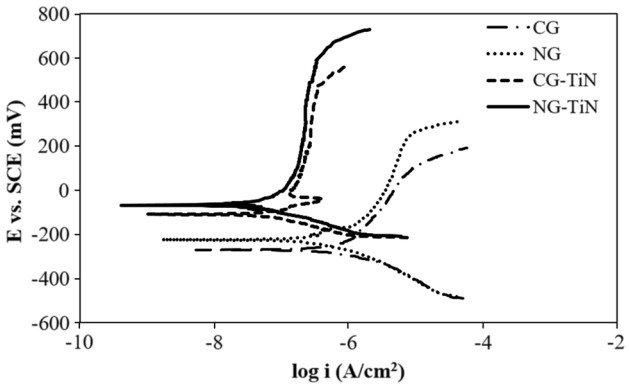

Fig. 13 Potentiodynamic polarization curves of NG and CG with and without TiN coating in 3.5% NaCl solution

was easier. Therefore, a more compact passive layer could be formed on the surface. This suggests that the fine-grained structure can affect the structure of the passive film formed on the surface of the 301 steel. Jinlong et al. [52] showed that ultrafine-grained structure induced by cold rolling and annealing increased the corrosion resistance of 2205 duplex stainless steel. By applying the coating, the curves have a large shift towards the lower current densities, and the corrosion potential is more positive. Increasing the potential by applying TiN coating on 316 stainless steel in sulphuric acid medium has previously been reported [56, 57]. Based on Fig. 13, the coated NG sample shows higher breakdown potential and also lower corrosion and passive current densities. This illustrates the higher corrosion resistance of the coated NG sample.

The electrochemical parameters obtained from the analysis of polarization curves are listed in Table 3. According to this table, with the grain refinement of 301 steel, the corrosion current density was decreased from 1.92 to 1.32 $\mu A/cm^2$. On the other hand, by applying TiN coating on the NG sample, the corrosion current density was reached one-tenth of the uncoated condition. The simultaneous effect of grain refinement and coating reduced the corrosion current density to 0.14 $\mu A/cm^2$. Compared to the best results of the most recent similar research (0.25 $\mu A/cm^2$ corrosion current density) for TiN coatings on stainless steel [58], this results showed a decrease in the corrosion current density. Improvement in corrosion behavior is also

Table 3 Electrochemical parameters obtained from potentiodynamic measurement different samples in 3.5% NaCl

Sample	E_{corr} versus SCE (mV)	i_{corr} (μA/cm^2)	$i_{passive}$ (μA/cm^2)	$E_{breakdown}$ versus SCE (mV)
CG	−268.1	1.92	3.31	102
NG	−227	1.32	2.50	214
CG-TiN	−110	0.20	0.21	470
NG-TiN	−67	0.14	0.19	544

evident by comparing the values of breakdown potential and passive current density. As mentioned before, in addition to the formation of a passive film, this can be attributed to the formation of a thicker and more compact TiN coating on the NG substrate.

4 Conclusions

Titanium nitride films were deposited onto nano- and coarse-grained AISI 301 stainless steel sheets using the cathodic arc evaporation method. The main conclusions are as follows:

- The thickness of the coating in nano- and coarse-grained samples was estimated to be 1.81 and 0.257 μm, respectively. Such a large difference in the coating thickness was attributed to the epitaxial growth of the coating on the substrates. It can be said that a reduction in grain size can increase the speed of coating and therefore increase the efficiency of the coating process.
- The XRD pattern of both samples showed the same reflections of TiN with a similar preferred orientation along the (111) plane.
- Coating exhibits an excellent adhesion quality to both substrates. Also, good stability of the coating adhesion was observed after 7 days of immersion in a 3.5% NaCl solution.
- The corrosion resistance was improved by applying TiN coating on the samples, and the corrosion resistance of the coated NG sample is better than that of the coarse grain which represents less penetration of corrosive ions in the coating.

Declarations

Conflict of interest On behalf of all authors, the corresponding author states that there is no conflict of interest.

References

1. M. Odnobokova, A. Belyakov, R. Kaibyshev, Philos. Mag. **99**, 531 (2019). https://doi.org/10.1080/14786435.2018.1546961
2. D. Rasouli, A. Kermanpur, E. Ghassemali, A. Najafizadeh, Met. Mater. Int. **25**, 846 (2019). https://doi.org/10.1007/s12540-019-00255-w
3. M. Karimi, A. Najafizadeh, A. Kermanpur, M. Eskandari, Mater. Charact. **61**, 1220 (2009). https://doi.org/10.1016/j.matchar.2009.04.014
4. H. Wu, G. Niu, J. Cao, M. Yang, Mater. Sci. Technol. **33**, 480 (2017). https://doi.org/10.1080/02670836.2016.1229092
5. J.-B. Lee, I.H. Oh, Met. Mater. Int. **20**, 629 (2014). https://doi.org/10.1007/s12540-014-4007-0
6. H.-C. Choe, Y.-M. Ko, H.-O. Park, Met. Mater. Int. **12**, 365 (2006). https://doi.org/10.1007/BF03027555
7. T. Abubakar, M. Rahman, D.P. Dowling, J. Stokes, M.S.J. Hashmi, Surf. Eng. **26**, 499 (2010). https://doi.org/10.1179/174329409X433885
8. D.M. Sanders, A. Anders, Surf. Coat. Tech. **133-134**, 78 (2000). https://doi.org/10.1016/S0257-8972(00)00879-3
9. A. Erdemir, A.A. Voevodin, in *Handbook of Deposition Technologies for Films and Coatings*, 3rd edn., ed. by P.M. Martin (William Andrew Publishing, Norwich, 2010), pp. 679–715
10. M. Ali, E.B. Hamzah, I.A. Qazi, M.R.M. Toff, Curr. Appl. Phys. **10**, 471 (2010). https://doi.org/10.1016/j.cap.2009.07.007
11. M. Ali, E.B. Hamzah, M.R.M. Toff, Surf. Rev. Lett. **13**, 621 (2006). https://doi.org/10.1142/S0218625X0600858X
12. A. Shah, S. Izman, M.R. Abdul Kadir, H. Mas-Ayu, M. Anwar, A.B. Ma'aram, Adv. Mater.Res. **845**, 436 (2013). https://doi.org/10.4028/www.scientific.net/AMR.845.436
13. M. Ali, E.B. Hamzah, I.A. Qazi, M.R.M. Toff, Mater. Sci. Forum **636-637**, 965 (2010). https://doi.org/10.4028/www.scientific.net/MSF.636-637.965
14. M. Ali, E. Hamzah, M.R.M. Toff, Mater. Sci. Eng. A **474**, 236 (2008). https://doi.org/10.1016/j.msea.2007.04.030
15. M.A. Hussein, A.M. Kumar, N. Ankah, M.A. Azeem, Ceram. Int. **47**, 23203 (2021). https://doi.org/10.1016/j.ceramint.2021.05.032
16. M. Eskandari, A. Najafizadeh, A. Kermanpur, M. Karimi, Mater. Design **30**, 3869 (2009). https://doi.org/10.1016/j.matdes.2009.03.043
17. VDI 3198, Coating (CVD, PVD) of cold forging tools (Verein Deutscher Ingenieure (VDI), Dusseldorf, 1992), p. 7
18. L. Hultman, H.T.G. Hentzell, J.E. Sundgren, B.O. Johansson, U. Helmersson, Thin Solid Films **124**, 163 (1985). https://doi.org/10.1016/0040-6090(85)90259-7
19. M. Leoni, P. Scardi, S. Rossi, L. Fedrizzi, Y. Massiani, Thin Solid Films **345**, 263 (1999). https://doi.org/10.1016/S0040-6090(98)01741-6
20. L. De Schepper, M. D'Olieslaeger, G. Knuyt, L.M. Stals, M. Van Stappen, B. Malliet, J.P. Celis, J.R. Roos, Thin Solid Films **173**, 199 (1989). https://doi.org/10.1016/0040-6090(89)90135-1
21. A. Mubarak, E.B. Hamzah, M.R.H.M. Toff, Surf. Rev. Lett. **14**, 93 (2007). https://doi.org/10.1142/S0218625X07009104
22. P. Harlin, P. Carlsson, U. Bexell, M. Olsson, Surf. Coat. Tech. **201**, 4253 (2006). https://doi.org/10.1016/j.surfcoat.2006.08.103
23. K.V. Smyrnova, A.D. Pogrebnjak, V.M. Beresnev, S.V. Litovchenko, S.O. Borba-Pogrebnjak, A.S. Manokhin, S.A. Klimenko, B. Zhollybekov, A.I. Kupchishin, Y.O. Kravchenko, O.V. Bondar, Met. Mater. Int. **24**, 1024 (2018). https://doi.org/10.1007/s12540-018-0110-y
24. A. Mubarak, P. Akhter, E. Hamzah, M.R.H. Mohd Toff, I.A. Qazi, Surf. Rev. Lett. **15**, 401 (2008). https://doi.org/10.1142/S0218625X08011524

25. M. Łępicka, M. Grądzka-Dahlke, D. Pieniak, K. Pasierbiewicz, A. Niewczas, Wear **382–383**, 62 (2017). https://doi.org/10.1016/j.wear.2017.04.017
26. M. Łępicka, M. Grądzka-Dahlke, D. Pieniak, K. Pasierbiewicz, K. Kryńska, A. Niewczas, Wear **422–423**, 68 (2019). https://doi.org/10.1016/j.wear.2019.01.029
27. S.C. Vettivel, R. Jegan, J. Vignesh, S. Suresh, Surf. Interfaces **6**, 1 (2017). https://doi.org/10.1016/j.surfin.2016.10.008
28. I. Pana, V. Braic, M. Dinu, E.S.M. Mouele, A.C. Parau, L.F. Petrik, M. Braic, Coatings **10**, 710 (2020). https://doi.org/10.3390/coatings10080710
29. D.H. Buckley, *Surface Effects in Adhesion, Friction, Wear, and Lubrication*, 1st edn (Elsevier, Amsterdam, 1981), pp. 127–128
30. M.T. Laugier, J. Vac. Sci. Technol. A **5**, 67 (1987). https://doi.org/10.1116/1.574139
31. E.L. Dalibón, J.N. Pecina, M.N. Moscatelli, M.A. Ramírez Ramos, V.J. Trava-Airoldi, S.P. Brühl, J. Bio-Tribo-Corros. **5**, 34 (2019). https://doi.org/10.1007/s40735-019-0228-6
32. C.H. Hsu, K.H. Huang, M.R. Lin, Surf. Coat. Tech. **259**, 167 (2014). https://doi.org/10.1016/j.surfcoat.2014.02.001
33. Y. Ma, J. Yang, X. Tian, C. Gong, W. Zheng, Y. He, Z. Gao, J. Adhes, Sci. Technol. **34**, 1040 (2020). https://doi.org/10.1080/01694243.2019.1690774
34. J. Gerth, U. Wiklund, Wear **264**, 885 (2008). https://doi.org/10.1016/j.wear.2006.11.053
35. W. Heinke, A. Leyland, A. Matthews, G. Berg, C. Friedrich, E. Broszeit, Thin Solid Films **270**, 431 (1995). https://doi.org/10.1016/0040-6090(95)06934-8
36. P.C. Jindal, D.T. Quinto, G.J. Wolfe, Thin Solid Films **154**, 361 (1987). https://doi.org/10.1016/0040-6090(87)90379-8
37. M. Bozorg, A. Ramezani, Mater. Corros. **68**, 725 (2017). https://doi.org/10.1002/maco.201609347
38. M. Cui, J. Pu, G. Zhang, L. Wang, Q. Xue, RSC Adv. **6**, 28570 (2016). https://doi.org/10.1039/C6RA05527C
39. G.I. Ramírez-Peralta, U. León-Silva, M.E. Nicho Díaz, M.G. Valladares-Cisneros, Mater. Corros. **69**, 1631 (2018). https://doi.org/10.1002/maco.201810119
40. N. Nemati, M. Bozorg, O.V. Penkov, D.-G. Shin, A. Sadighzadeh, D.-E. Kim, ACS Appl. Mater. Interfaces **9**, 30149 (2017). https://doi.org/10.1021/acsami.7b08565
41. K.D. Ralston, N. Birbilis, Corrosion **66**, 075005 (2010). https://doi.org/10.5006/1.3462912
42. M. Thomas, T. Lindley, D. Rugg, M. Jackson, Acta Mater. **60**, 5040 (2012). https://doi.org/10.1016/j.actamat.2012.06.017
43. M. Ran, C. Zhang, L. Wen, H. Zhou, W. Zheng, Surf. Eng. **37**, 739 (2021). https://doi.org/10.1080/02670844.2020.1790157
44. Y.B. Lei, Z.B. Wang, B. Zhang, Z.P. Luo, J. Lu, K. Lu, Acta Mater. **208**, 116773 (2021). https://doi.org/10.1016/j.actamat.2021.116773
45. S.V. Phadnis, A.K. Satpati, K.P. Muthe, J.C. Vyas, R.I. Sundaresan, Corros. Sci. **45**, 2467 (2003). https://doi.org/10.1016/S0010-938X(03)00099-4
46. A. Fattah-Alhosseini, S. Vafaeian, J. Alloy. Compd. **639**, 301 (2015). https://doi.org/10.1016/j.jallcom.2015.03.142
47. T. Fu, Z. Zhan, L. Zhang, Y. Yang, Z. Liu, J. Liu, L. Li, X. Yu, Surf. Coat. Tech. **280**, 129 (2015). https://doi.org/10.1016/j.surfcoat.2015.08.041
48. T. Balusamy, S. Kumar, T.S.N. Sankara Narayanan, Corros. Sci **52**, 3826 (2010). https://doi.org/10.1016/j.corsci.2010.07.004
49. B. Thangaraj, S.N.T.S. Nellaiappan, R. Kulandaivelu, M.H. Lee, T. Nishimura, ACS Appl. Mater. Interfaces **7**, 17731 (2015). https://doi.org/10.1021/acsami.5b03877
50. A.A. Aghuy, M. Zakeri, M.H. Moayed, M. Mazinani, Corros. Sci. **94**, 368 (2015). https://doi.org/10.1016/j.corsci.2015.02.024
51. X. Fu, Y. Ji, X. Cheng, C. Dong, Y. Fan, X. Li, Mater. Today Commun. **25**, 101429 (2020). https://doi.org/10.1016/j.mtcomm.2020.101429
52. L. Jinlong, L. Tongxiang, W. Chen, D. Limin, Mater. Sci. Eng. C **62**, 558 (2016). https://doi.org/10.1016/j.msec.2016.02.008
53. N. Imaz, M. Ostra, M. Vidal, J.A. Díez, M. Sarret, E. García-Lecina, Corros. Sci. **78**, 251 (2014). https://doi.org/10.1016/j.corsci.2013.10.005
54. S. Ammar, K. Ramesh, I.A.W. Ma, Z. Farah, B. Vengadaesvaran, S. Ramesh, A.K. Arof, Surf. Coat. Tech. **324**, 536 (2017). https://doi.org/10.1016/j.surfcoat.2017.06.014
55. O. Teschke, M.U. Kleinke, F. Galembeck, J. Electrochem. Soc. **135**, 2188 (1988). https://doi.org/10.1149/1.2096237
56. K. Feng, Y. Shen, J. Mai, D. Liu, X. Cai, J. Power Sources **182**, 145 (2008). https://doi.org/10.1016/j.jpowsour.2008.03.088
57. M.M. Ghorbani, R. Taherian, M. Mohammadi, M. Bozorg, Surf. Eng. **37**, 822 (2021). https://doi.org/10.1080/02670844.2020.1827943
58. Q. Wan, H. Ding, M.I. Yousaf, Y.M. Chen, H.D. Liu, L. Hu, B. Yang, Thin Solid Films **616**, 601 (2016). https://doi.org/10.1016/j.tsf.2016.08.005